

Thermal conductivity of the quasi-1D materials TaSe₃ and ZrTe₃

Topojit Debnath,^{*} Bishwajit Debnath,[†] and Roger K. Lake[‡]

*Department of Electrical and Computer Engineering,
University of California, Riverside, CA 92521, USA*

The high breakdown current densities and resilience to scaling of the metallic transition metal trichalcogenides TaSe₃ and ZrTe₃ make them of interest for possible interconnect applications, and it motivates this paper of their thermal conductivities and phonon properties. These crystals consist of planes of strongly bonded one-dimensional chains more weakly bonded to neighboring chains. Phonon dispersions and the thermal conductivity tensors are calculated using density functional theory combined with an iterative solution of the phonon Boltzmann transport equation. The phonon velocities and the thermal conductivities of TaSe₃ are considerably more anisotropic than those of ZrTe₃. The maximum longitudinal-acoustic velocity in ZrTe₃ occurs in the cross-chain direction, and this is consistent with the strong cross-chain bonding that gives rise to large Fermi velocities in that direction. The thermal conductivities are similar to those of other metallic two-dimensional transition metal dichalcogenides. At room temperature, a significant portion of the heat is carried by the optical modes. In the low frequency range, the phonon lifetimes and mean free paths in TaSe₃ are considerably shorter than those in ZrTe₃. The shorter lifetimes in TaSe₃ are consistent with the presence of lower frequency optical branches and zone-folding features in the acoustic branches that arise due to the doubling of the TaSe₃ unit cell within the plane.

I. INTRODUCTION

The transition metal trichalcogenides (TMTs) have a quasi-one-dimensional (quasi-1D) crystalline structure that can give rise to quasi-1D behavior of the electronic and phononic properties [1–3]. The lattice structures of TMTs consist of a transition metal (M) atom, contained at the center of a prism of chalcogen (X) atoms [4]. The MX_3 prisms create strongly M - X covalently bonded chains arranged side-by-side via longer, weaker M - X bonds, and planarly stacked with even weaker van der Waals type X - X bonds which effectively makes these materials two-dimensional layers of quasi-1D chains [5], giving them the apt name of quasi-1D materials. The crystalline anisotropy gives rise to directional anisotropy in electrical, optical, phononic, and thermal properties [6–12].

The low dimensionality of the MX_3 materials makes them particularly susceptible to multiple phase transitions such as superconductivity [13–16] and charge density wave (CDW) formation [17–20]. The latter has motivated extensive, prolonged research into CDW transitions [1, 21–23], sliding [24, 25], dynamics [26–30], dimensional scaling [31–38] in the metallic TMTs, and their use for device applications [39–42]. The Fermi surface nesting, CDW, and their signatures in the phonon spectrum of ZrTe₃ are a topic of ongoing interest [43–53]. Inelastic x-ray scattering revealed a Kohn anomaly in the transverse acoustic (TA) phonon of ZrTe₃ at the CDW wavevector for temperatures up to 292 K [47]. As the temperature was reduced to and below T_{CDW} , partial Fermi surface

splitting was observed by angle-resolved photoelectron spectroscopy [46, 48].

There has been a recent resurgence of interest in 1D and quasi-1D materials, in part motivated by, and evolving from, the intense interest in two-dimensional (2D) van der Waals materials. Reference [54] provides a review of the more recent work on the transition metal trichalcogenides. The direct gap semiconductor TiS₃ has received much attention after it was exfoliated to few layer thicknesses and shown to have a high photo-response with a bandgap of 1.1 eV [55]. Investigations of few layer and nanoribbon TiS₃ transistors followed, and experimentally extracted mobilities were in the range of 20-70 cm²V⁻¹s⁻¹ [9, 56–59]. BN encapsulation of 26 nm thick TiS₃ resulted in two and four terminal room-temperature mobilities of 54 and 122 cm²V⁻¹s⁻¹, respectively [60]. The properties of the MX_3 materials with $M = \text{Ti, Zr, Hf}$, and $X = \text{S, Se, Te}$, have been investigated with density functional theory (DFT) to determine electronic structure, bandgaps, specific heats, and elastic constants [61]. Exploiting the anisotropy inherent in TMTs has been proposed for application in next generation electronics, contacts, polarizers and photo-detectors [62, 63].

The metallic TMTs have also received renewed attention after it was discovered that the breakdown current densities of TaSe₃ (~ 10 MA/cm² where MA represents mega-amperes) and ZrTe₃ (~ 100 MA/cm²) are higher than that of Cu [64, 65]. Furthermore, in contrast to Cu wires, the resistivity of TaSe₃ did not degrade as the cross-sectional dimensions were scaled down to 10 nm [66]. This was attributed to the single crystalline nature of the nanowires and the self-passivation of the surfaces that eliminate grain-boundary and surface roughness scattering. Because of these properties, metallic TMTs were proposed for local interconnect applications in nano-scaled electronics [64, 66].

Since the metallic TMTs can carry record current den-

^{*} tdebn001@ucr.edu

[†] Current affiliation : Intel Corporation, Hillsboro, Oregon

[‡] Corresponding author: rlake@ece.ucr.edu

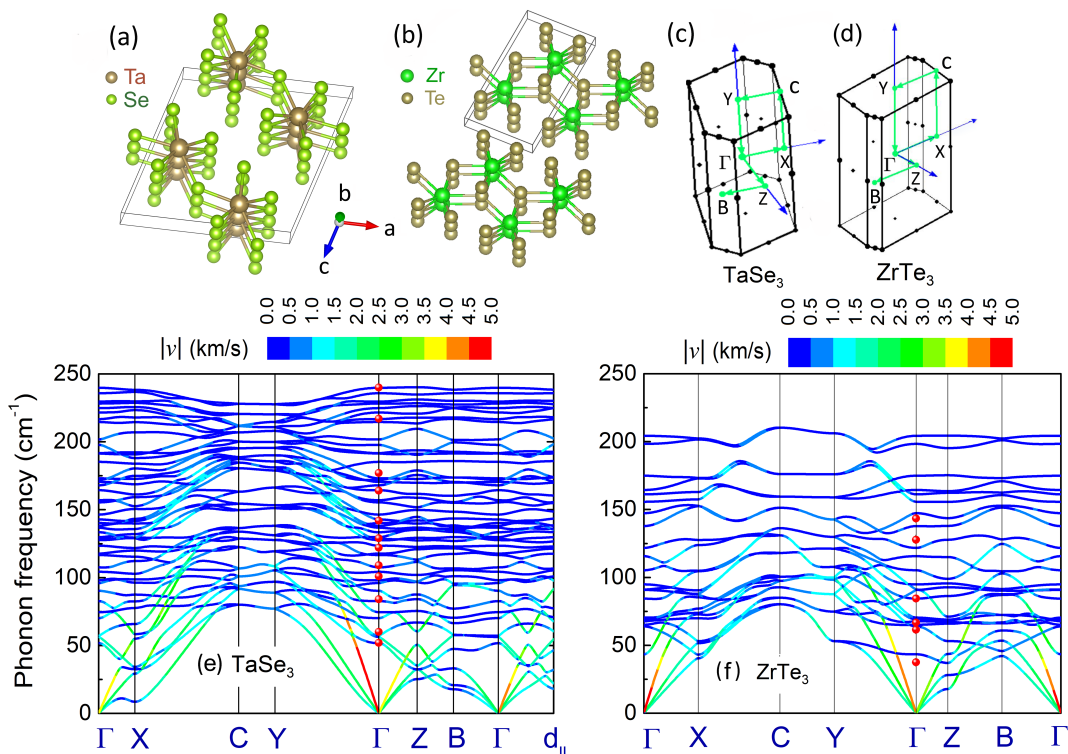


FIG. 1. Crystal structures and unit cells of (a) TaSe_3 , (b) ZrTe_3 , and the corresponding Brillouin zones (BZs) for (c) TaSe_3 and (d) ZrTe_3 . The wires grow along the b axis. Lattice vectors a and b lie along the x and y axes, respectively. Lattice vector c lies at angles β with respect to the x -axis with values of 106.36° and 97.95° for TaSe_3 and ZrTe_3 , respectively. Phonon dispersions of bulk (e) TaSe_3 and (f) ZrTe_3 . The color indicates the magnitude of the group velocity as given in the color bar. The directions in the Brillouin zone are shown in (c) and (d). The red spheres indicate experimental Raman peaks at 300 K [71, 72]. For both crystals, $\Gamma - Y$ is the chain direction. For TaSe_3 , $\Gamma - B$ is the cross-plane direction, and $\Gamma - d_{\parallel}$ is the cross-chain direction, where $d_{\parallel} = (\mathbf{a}^* + 0.8536\mathbf{c}^*)/2$. For ZrTe_3 , $\Gamma - Z$ is the cross-plane direction. $\Gamma - X$ is 8.0° off from the cross-chain direction, however the differences in dispersions between the true cross-chain direction and $\Gamma - X$ are negligible.

sities and have been proposed for interconnect applications, it is necessary to also understand their thermal transport properties. A secondary motivation to explore the thermal transport properties of low-dimensional materials is their potential of exhibiting higher thermoelectric efficiency [67]. Recently, a high thermoelectric figure of merit was predicted for monolayer ZrSe_3 resulting from a high power factor and relatively low thermal conductivity [68].

Although the electronic structure and the electronic transport properties of quasi-1D materials have been extensively studied, their phononic and thermal transport properties have received less attention. Recently, a thermal conductivity of $7 \text{ W m}^{-1} \text{ K}^{-1}$ was measured in bulk polycrystalline ZrTe_3 [69]. A DFT investigation of monolayer ZrSe_3 found room temperature thermal conductivities parallel to the chain direction of $8 \text{ W m}^{-1} \text{ K}^{-1}$ and perpendicular to the chain direction of $3 \text{ W m}^{-1} \text{ K}^{-1}$ [68]. A recent study of TiS_3 found room temperature thermal conductivities of $5.78 \text{ W m}^{-1} \text{ K}^{-1}$ and $2.84 \text{ W m}^{-1} \text{ K}^{-1}$ along the chain and interchain directions, respectively [70].

In this paper, we calculate the phonon modes of TaSe_3

and ZrTe_3 , using DFT. We determine the anisotropic velocities of the acoustic branches along the high-symmetry directions, and we compare the frequencies of the optical modes to experimental Raman frequencies and determine the associated mode displacements. We then solve the phonon Boltzmann transport equation (PBTE) to determine the lattice thermal conductivities and to investigate the phonon lifetimes and mean free paths in these two quasi-1D materials.

II. CRYSTALLOGRAPHIC STRUCTURES AND PROPERTIES

Because the TMTs consist of planes of 1D chains of strongly bonded trigonal MX_3 prisms with each chain bonded to its neighbor chain through longer, weaker M-X bonds and each plane bonded to its neighbor plane through even weaker van der Waals type bonds, we define three different directions: chain, cross-chain (cc), and cross-plane (cp). The chain direction is parallel to the 1D chains and along the \mathbf{b} lattice vector for both crystals as shown in Fig. 1. The cross-chain direction is perpendicular

ular to the 1D chains and within the same van der Waals plane, and the cross-plane direction is perpendicular to the van der Waals planes.

TaSe₃ and ZrTe₃ are metallic with monoclinic crystal structures belonging to space group P2₁/m. Both crystals have inversion symmetry so that the phonon modes at Γ have either even or odd parity. The experimentally determined lattice constants of TaSe₃ are $a = 10.411$ Å, $b = 3.494$ Å, $c = 9.836$ Å, and $\beta = 106.36^\circ$; and those of ZrTe₃ are $a = 5.895$ Å, $b = 3.926$ Å, $c = 10.104$ Å, and $\beta = 97.93^\circ$ as shown in Fig. 1(a,b).[73] The van der Waals gaps are visible, and the interchain metal-chalcogen bond is longer than the intrachain metal-chalcogen bond. The unit cell of TaSe₃ contains 16 atoms, and the unit cell of ZrTe₃ contains 8 atoms. The electrical conductivity along the chain direction of TaSe₃ at room temperature is reported to be $\sim 1.7 \times 10^5$ (Ωm)⁻¹ [14] and it remains metallic down to liquid He temperatures [13, 14]. ZrTe₃ undergoes a CDW phase transition at $T_{CDW} = 63$ K [44, 74]. For that reason, we limit our thermal conductivity calculations to temperatures 100 K and above.

The structural and electronic properties of ZrTe₃ have been investigated extensively both experimentally and theoretically [44, 45, 75]. The electrical conductivity of ZrTe₃ is highest in the *cross-chain* direction (along the direction of the \mathbf{a} lattice vector), and, depending on the experimental work, it is a factor of 1.4 to 1.9 larger than the conductivity in the *chain* direction (along the \mathbf{b} lattice vector) [45, 75]. At $T = 300$ K, experimental values of the electrical conductivity measured along the a -axis are 5.6×10^5 (Ωm)⁻¹ [75] and 1.3×10^6 (Ωm)⁻¹ [45]; and the values measured along the b -axis are 4.0×10^5 (Ωm)⁻¹ [75] and 6.9×10^5 (Ωm)⁻¹ [45]. This is a result of Te-Te σ and σ^* bands formed from Te p_x orbitals. The intrachain Te-Te distance is 2.80 Å, and the cross-chain distance is 3.10 Å allowing for Te-Te bonding that results in highly dispersive electronic bands. We will see a similar anisotropy in the acoustic phonon velocities with the highest velocity also occurring in the *cross-chain* direction.

To investigate the effect of crystal anisotropy, we calculate the phonon dispersions and the acoustic phonon velocities along the chain, cross-chain, and cross-plane directions. The chain direction always corresponds to the \mathbf{b}^* reciprocal lattice vector and the $\Gamma - Y$ paths in the Brillouin zones shown in Fig. 1(c,d). For ZrTe₃, the cross-chain direction also corresponds to the \mathbf{a} lattice vector in Fig. 1(b) and the \hat{x} direction in Cartesian coordinates. The cross-plane direction is perpendicular to \mathbf{a} and therefore parallel to the \mathbf{c}^* reciprocal lattice vector. Thus, for ZrTe₃, the phonon dispersion in the cross-plane direction is along the $\Gamma - Z$ path in the Brillouin zone shown in Fig. 1(d). The closest high symmetry line in the Brillouin zone to the cross-chain direction (\hat{x}) is $\Gamma - X$ and this differs from \hat{x} by 8.0° for ZrTe₃. In terms of the reciprocal lattice vectors, the \hat{x} direction for ZrTe₃ is $\mathbf{a}^* - 0.2353\mathbf{c}^*$.

For TaSe₃, the \mathbf{a} and \mathbf{c} lattice vectors have both cross-chain and cross-plane components, and the \mathbf{a} lattice vector points in the \hat{x} direction. The cross-chain direction is in the direction of the sum of the lattice vectors $\mathbf{a} + \mathbf{c}$. [76] The cross-plane direction is perpendicular to $\mathbf{a} + \mathbf{c}$ and therefore in the direction of $\mathbf{b} \times (\mathbf{a} + \mathbf{c}) \propto (\mathbf{a}^* - \mathbf{c}^*)$ where \mathbf{a}^* and \mathbf{c}^* are the reciprocal lattice vectors in the $x - y$ plane. Thus, for TaSe₃, the phonon dispersion in the cross-plane direction is along the $\Gamma - B$ path in the Brillouin zone shown in Fig. 1(c). The closest high symmetry line in the Brillouin zone to the cross-chain direction is along $\mathbf{a}^* + \mathbf{c}^*$ which runs between Γ and the corner of the X and Z faces in Fig. 1(c). This differs from the true cross chain direction by 3.4° . The true cross chain direction is $\mathbf{a}^* + 0.8536\mathbf{c}^*$.

III. METHODS

Structural optimization of each material is performed using density functional theory with projector-augmented-wave (PAW) method [77] and Perdew-Burke-Ernzerhof (PBE) exchange correlation functionals [78], as implemented in the Vienna ab initio simulation package (VASP) [79, 80]. The van der Waals interactions are included by semi-empirical correction of Grimme-D2 [81]. Converged Monkhorst-Pack grids of $9 \times 9 \times 3$ are used for TaSe₃ and ZrTe₃. All structures are relaxed until the forces on each atom is less than 10^{-5} eV/Å and the energy convergence reaches 10^{-8} eV. The relaxed lattice constants of TaSe₃ and ZrTe₃ are within 1% of the experimentally reported values. The magnitudes and angles are provided in the Appendix along with the calculated electronic dispersion.

To obtain the phonon frequency dispersion and other thermodynamics properties, the second-order (harmonic) interatomic force constants (IFCs) are required. The second-order IFCs are calculated using the finite-displacement, supercell approach as implemented in PHONOPY [82, 83]. For the phonon dispersion of TaSe₃ and ZrTe₃, a supercell size of $2 \times 2 \times 2$, has been used, with a K-point grid of $2 \times 6 \times 2$ and $6 \times 6 \times 4$, respectively.

The thermal conductivity tensor is calculated from the phonon Boltzmann transport equation, within the three-phonon scattering approximation as implemented within ShengBTE, [84, 85]

$$\kappa_{\alpha\beta} = \frac{1}{k_B T^2 N V} \sum_{\lambda} f_{\lambda}^0 (f_{\lambda}^0 + 1) (\hbar \omega_{\lambda})^2 v_{\lambda}^{\alpha} F_{\lambda}^{\beta}. \quad (1)$$

In Eq. (1), ω_{λ} is the phonon energy of each phonon mode λ , f_{λ}^0 is the equilibrium Bose-Einstein distribution of that mode and v_{λ} is the group velocity. λ represents both the phonon branch index p and wave vector \mathbf{q} . V is the volume and N is the number of \mathbf{q} points in the irreducible Brillouin zone. The quantity $F_{\lambda}^{\beta} = \tau_{\lambda}^0 (v_{\lambda}^{\beta} + \Delta_{\lambda}^{\beta})$ where τ_{λ}^0 is the lifetime in the relaxation-time approximation (RTA), and Δ_{λ}^{β} is a correction to the RTA from an iterative solution of the PBTE. Full details of the theory

TABLE I. Velocity (m/s) of LA and TA modes near Γ along four high symmetry directions and the exact cross-chain direction labeled as \mathbf{d}_{cc} . The chain direction is $\Gamma - Y$. The cross-plane direction is $\Gamma - B$ for TaSe₃ and $\Gamma - Z$ for ZrTe₃. The first row for each mode corresponds to the velocities at Γ . If the maximum velocity occurs at finite frequency, its value and corresponding frequency (cm⁻¹) are provided in the second row. A ‘-’ in the second row indicates that the maximum velocity occurs at Γ .

Material	Mode	$\Gamma - X$	$\Gamma - Y$	$\Gamma - Z$	$\Gamma - B$	\mathbf{d}_{cc}
TaSe ₃	LA	3962	4956	3814	2342	4105
	TA ₁	1558	1256	2000	1467	1824
		-	2143 (35.6)	-	-	-
	TA ₂	2374	2294	2446	1963	2481
		-	2409 (38.0)	-	-	-
ZrTe ₃	LA	4723	4343	3256	4686	4734
	TA ₁	1618	1629	1562	1634	1511
		-	1829 (23.1)	-	1651 (13.5)	-
	TA ₂	2127	2406	2257	2391	2081
		-	2563 (37.4)	-	-	-

are described in Ref. [84]. Diagonal elements of κ along other directions are obtained by a unitary transformation (rotation) of the thermal conductivity tensor.

The calculation of the three-phonon matrix elements, needed for the calculation of τ_{λ}^0 and Δ_{λ}^{β} [84], requires the third-order (anharmonic) IFCs. A $2 \times 2 \times 1$ supercell is used to calculate the anharmonic IFCs, which generates 3472 and 520 atomic structure configurations for TaSe₃ and ZrTe₃, respectively. Atomic interactions up to fifth-nearest neighbor are considered. Both the RTA and full iterative approach, are used to solve the phonon BTE, as implemented in the ShengBTE package [84, 86]. In the iterative approach, κ is converged to a precision of 10^{-5} between iterative steps. Convergence with respect to the k-point grid is also checked. The converged Monkhorst-Pack grids are $14 \times 14 \times 6$ for TaSe₃ and $8 \times 14 \times 8$ for ZrTe₃.

IV. RESULTS AND DISCUSSIONS

A. Phonon dispersion

The phonon dispersions of TaSe₃ and ZrTe₃ are shown in Fig. 1(e,f). The color scheme indicates the absolute group velocity at each phonon \mathbf{q} -vector and phonon branch with the magnitudes given by the color bars. The large number of atoms in the unit cells result in many low-frequency optical modes. A number of the optical modes are highly dispersive. Experimentally, the many optical modes create complex Raman spectra with closely spaced peaks. The red circles indicate the peaks from experimental Raman data.[71, 72] Most of the experimental Raman peaks match well with the DFT calculated phonon frequencies at Γ as shown in Fig. 1(e,f). The experimental and calculated values are listed in the Supplementary Information along with images of the displacements and symmetry of each mode at Γ . Below, we first discuss the anisotropy of the acoustic modes, and then

we discuss the nature of several of the lower frequency, dispersive optical modes.

The anisotropy of the transition metal trichalcogenides has been a topic of long-term interest. The degree with which a crystal behaves as quasi-1D or 2D depends on the strength of the interchain coupling, and the interchain coupling manifests itself in the directional dispersions of both the electrons and phonons. Larger coupling results in more dispersive bands and higher velocities. Thus, the phonon velocities give one measure of the anisotropy of the crystals. The velocities of the three acoustic modes along four high symmetry lines of the Brillouin zone and the exact cross-chain direction are given in Table I.

For these crystals, the LA velocities along the chain directions ($\Gamma - Y$) are high, and for TaSe₃, they are the maximum velocities among all modes and all directions, as one would expect from a quasi-1D crystal structure. For ZrTe₃, the highest velocity phonon is the LA mode in the *cross-chain* direction. This is consistent with its electronic anisotropy in which the highest Fermi velocities occur for the Te p_x bands in the cross-chain direction (electronic structure plots are shown in the Appendix).

The maximum velocities of the TA shear modes are highest along the chain directions for these crystals, with the one exception of the TA₂ mode of TaSe₃ which has its highest velocity in the cross-chain direction. Also, there is more nonlinearity to the TA mode dispersions, such that the maximum velocities of the TA modes occur at a finite frequency on the order of 1 THz.

Finally, the lowest velocity LA modes for both crystals are in the cross-plane direction. For TaSe₃, the lowest velocity TA modes are also in the cross-plane direction, and for ZrTe₃, the lowest velocity TA modes are in the cross-chain direction.

The acoustic phonon velocities exhibit different degrees of anisotropy for these two crystals. If we consider, for example, the LA mode, then its anisotropy in TaSe₃ is significantly larger than in ZrTe₃. For TaSe₃, the ratios

of the maximum velocities in the chain (v_y), cross-chain (v_{cc}), and cross-plane (v_{cp}) directions are $v_y/v_{cc} = 1.2$, $v_y/v_{cp} = 2.1$, and $v_{cc}/v_{cp} = 1.8$. For ZrTe_3 , the ratios are $v_{cc}/v_y = 1.09$, $v_{cc}/v_{cp} = 1.8$, and $v_y/v_{cp} = 1.3$. Every ratio in TaSe_3 is greater than or equal to the corresponding one in ZrTe_3 . The LA mode of both materials appears to be more quasi-two-dimensional rather than quasi-one-dimensional, since the in-plane anisotropy, as characterized by the ratio v_y/v_{cc} or v_{cc}/v_y , is considerably less than the cross-plane anisotropy as characterized by the ratios v_y/v_{cp} and v_{cc}/v_{cp} . The anisotropy of the maximum velocities of the TA modes is always less than that of the LA modes. For example, in TaSe_3 , the TA_1 velocity ratios are $v_y/v_{cc} = 1.2$, $v_y/v_{cp} = 1.5$, and $v_{cc}/v_{cp} = 1.2$; and the TA_2 ratios are $v_{cc}/v_y = 1.03$, $v_{cc}/v_{cp} = 1.3$, and $v_y/v_{cp} = 1.2$.

We now consider the optical modes. The vibrational modes of TaSe_3 , shown in Fig. 1(e), can be represented at Γ as [71],

$$\Gamma_{\text{TaSe}_3} = 8A_u + 8B_g + 16B_u + 16A_g. \quad (2)$$

The $8A_u + 8B_g$ modes have vibrations along the chain axis (b axis), and the $16B_u + 16A_g$ modes are polarized in the $\mathbf{a} - \mathbf{c}$ plane. Illustrations of the displacements of the modes based on the point group symmetry of the isolated chains are shown in Ref. [87]. For each mode at Γ , the frequency, symmetry and images of the displacements calculated for the periodic unit cell are provided in the Supplementary Information (SI). The measured Raman frequency taken from the literature is also listed for each A_g and B_g mode.

Relevant to thermal transport, there are several low-frequency optical modes that have relatively large dispersion along the chain ($\Gamma - Y$) direction with maximum velocities in the range of 1 – 1.5 km/s. The three low-frequency optical modes with the largest dispersions (highest velocities) are B_g or A_u modes with displacements along the chain direction. Modes 5 (56.3 cm^{-1}) (B_g), 6 (57.1 cm^{-1}) (A_u), and 8 (74.5 cm^{-1}) (B_g) at Γ (counting upwards from 0 frequency) are examples of such modes. Mode 4 (52.0 cm^{-1} , A_g), with displacements in the $a - c$ plane is slightly less dispersive immediately near Γ , but it has a relatively constant velocity of $\sim 1 \text{ km/s}$ along the entire $\Gamma - Y$ line. Above 75 cm^{-1} , the longitudinal acoustic mode appears to hybridize with many optical modes resulting in significant dispersion along $\Gamma - Y$ for modes between 75 cm^{-1} and 130 cm^{-1} .

The other types of optical modes are the A_g and B_u modes with either rotation or libration type non-collinear displacements in the $a - c$ plane perpendicular to the 1D chains. The 4th (51.7 cm^{-1}) (A_g), 7th (70.2 cm^{-1}) (A_u), and 9th (82.7 cm^{-1}) (A_g) modes at Γ correspond to such modes. In mode 4, each half of the unit cell, on either side of the van der Waals gap, has a rotational type displacement, and the rotational displacements of each half are out of phase by 180° . This is typical of all of the rotational type A modes with displacements on the

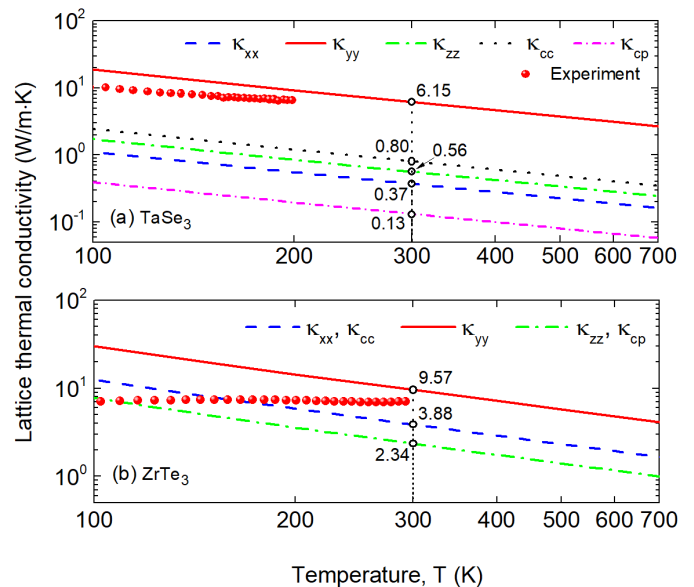


FIG. 2. The three diagonal components of the lattice thermal conductivity tensor versus temperature for (a) TaSe_3 and (b) ZrTe_3 . For TaSe_3 , the diagonal components of the transformed thermal conductivity tensor in the cross-chain (κ_{cc}) and cross-plane (κ_{cp}) directions are also shown. For ZrTe_3 , $\kappa_{cc} \equiv \kappa_{xx}$ and $\kappa_{cp} \equiv \kappa_{zz}$. The various components are indicated by the legends. The values for $T = 300 \text{ K}$ are labeled on the plots in units of $\text{Wm}^{-1}\text{K}^{-1}$. The red circles are experimental thermal conductivity values for (a) TaSe_3 and (b) polycrystalline ZrTe_3 taken from the literature [69, 88].

$\mathbf{a} - \mathbf{c}$ plane.

Fig. 1(f) shows the phonon dispersion of ZrTe_3 . For ZrTe_3 , there are 24 vibrational modes which can be represented at Γ as [72]

$$\Gamma_{\text{ZrTe}_3} = 4A_u + 4B_g + 8B_u + 8A_g. \quad (3)$$

Similar to TaSe_3 , the displacements of the $4A_u + 4B_g$ modes have vibrations along the chain (b) axis, and the $8B_u + 8A_g$ modes have displacements on the $a - c$ plane. There are 4 optical modes with relatively large dispersions along the chain ($\Gamma - Y$): modes 5 (64.0 cm^{-1} , B_g), 8 (69.1 cm^{-1} , B_g), 9 (70.4 cm^{-1} , A_g), and 12 (91.1 cm^{-1} , A_g). For ZrTe_3 , both types of displacements give rise to these relatively high velocity optical modes. Modes 5 and 8 have displacements along the chain and modes 9 and 12 have displacements on the $a - c$ plane. Between 75 cm^{-1} and 110 cm^{-1} , hybridization occurs between the longitudinal acoustic mode and the optical modes resulting in significant dispersion of the modes in that frequency window.

Although the highest velocity acoustic mode is in the cross-chain ($\Gamma - X$) direction, there are fewer dispersive optical modes along $\Gamma - X$ than in the chain direction. For this reason, the thermal conductivity is highest in the chain direction, since, as we shall see, a significant proportion of the heat is carried by the optical modes.

TABLE II. Thermal conductivities from this paper and from the literature.

Type	Materials	Thermal Conductivity ($\text{Wm}^{-1}\text{K}^{-1}$)	Remarks	Reference
Quasi-1D	TaSe ₃	6.2, 0.80, 0.13	Chain, cross-chain and cross-plane directions	This paper
	ZrTe ₃	9.6, 3.9, 2.3	Chain, cross-chain and cross-plane directions	This paper
	TaSe ₃	4.8	Experimental result (extrapolated to 300K)	[88]
	NbSe ₃	24	Bulk Material	[98]
	TiS ₃	5.8, 2.8	Chain and cross-chain	[70]
	ZrTe ₃	7	Bulk polycrystalline	[69]
	ZrTe ₅	11.2	Bulk material	[99]
	ZrTe ₅	3.9, 1.9, 0.4	Chain, cross-chain and cross-plane directions	[100]
	ZrTe ₅	2.2	Bulk polycrystalline	[101]
	HfS ₂	9	First principle study	[102]
	HfSe ₂	8	First principle study	[102]
	MoS ₂	1	Pristine	[103]
	MoSe ₂	0.9	Pristine	[103]
	2D	MoSe ₂	2.3	Compacted polycrystalline
MoTe ₂		1.9	Compacted polycrystalline	[104]
NbS ₂		11.8	Bulk material	[105]
NbSe ₂		2.1	Compacted polycrystalline	[104]
NbTe ₂		1.9	Compacted polycrystalline	[104]
TaS ₂		5	Bulk material	[106]
TaSe ₂		16	Bulk material	[106, 107]
TaSe ₂		1.7	Compacted polycrystalline	[104]
TaTe ₂		1.4	Compacted polycrystalline	[104]
TiS ₂		6.8, 4.2	In-plane and out-of-plane	[108]
WSe ₂		1.7	Compacted polycrystalline	[104]
WS ₂		2.2	Pristine	[103]
WSe ₂		0.8	Pristine	[103]
WTe ₂		1.6	Compacted polycrystalline	[104]
ZrSe ₂	10	First principle study	[102]	
ZrS ₂	18	First principle study	[102]	

B. Thermal conductivity

Figure 2 shows the lattice thermal conductivity for TaSe₃ and ZrTe₃ calculated from the PBTE using the full iterative approach. The iterative approach gives values slightly higher than those from the relaxation time approximation, and a comparison of the results from the two approaches is given in the Appendix. Below, we discuss the magnitudes and anisotropies of the thermal conductivities using the $T = 300$ K values shown in Fig. 2. The lattice thermal conductivities in the chain directions (κ_{yy}) of TaSe₃ and ZrTe₃, are $6.15 \text{ Wm}^{-1}\text{K}^{-1}$ and $9.57 \text{ Wm}^{-1}\text{K}^{-1}$, respectively. These values are similar to those of other metallic 2D TMD materials as shown in Table II. The calculated lattice thermal conductivities of TaSe₃ and ZrTe₃ follow a T^{-1} dependence expected when the thermal conductivity is limited by three-phonon scattering. [89] The diagonal elements of κ are fitted to the function $c_1 + c_2T^{-1}$, and the values of the coefficients are tabulated in the Appendix. The root mean square errors of all fits to the numerical data are less than $3 \times 10^{-15} \text{ Wm}^{-1}\text{K}^{-1}$.

The anisotropy of the thermal conductivity in TaSe₃, as indicated by the ratios $\kappa_{yy}/\kappa_{cc} = 7.7$ and $\kappa_{yy}/\kappa_{cp} = 47$ is large. For ZrTe₃, the anisotropy given by the ratios

$\kappa_{yy}/\kappa_{cc} = 2.5$ and $\kappa_{yy}/\kappa_{cp} = 4.1$ is considerably less. Unlike the electrical conductivity which is maximum in the cross-chain direction, the thermal conductivity of ZrTe₃ is maximum in the chain direction, even though the maximum phonon velocity occurs at very low frequencies for the LA mode in the cross-chain direction.

The experimental reports of thermal conductivity of quasi-1D materials are rare, due to the difficulty in measuring the thermal conduction in such ribbon-like geometries [88]. To our knowledge, only one experimental study of the thermal conductivity of TaSe₃ has been reported using a parallel thermal conductance (PTC) technique [90], and the data points are shown in Fig. 2(a)[88]. The experimental values are lower than the calculated values, and the comparison improves at higher temperatures when the phonon-phonon scattering mechanism starts to dominate. At $T = 200$ K, the experimental and calculated values are $6.62 \text{ Wm}^{-1}\text{K}^{-1}$ and $9.11 \text{ Wm}^{-1}\text{K}^{-1}$, respectively. From the experimental side, the accuracy of PTC technique to handle chain-structures like TaSe₃ is under question [88]. Missing from the calculations are the effects of impurities, surface scattering, finite grain sizes, and random isotopes [91]. For ZrTe₃, there is one reported measurement of the thermal conductivity in a bulk, polycrystalline sample with a value of $7 \text{ Wm}^{-1}\text{K}^{-1}$

at room temperature which is similar to our calculated value of $9 \text{ Wm}^{-1}\text{K}^{-1}$.

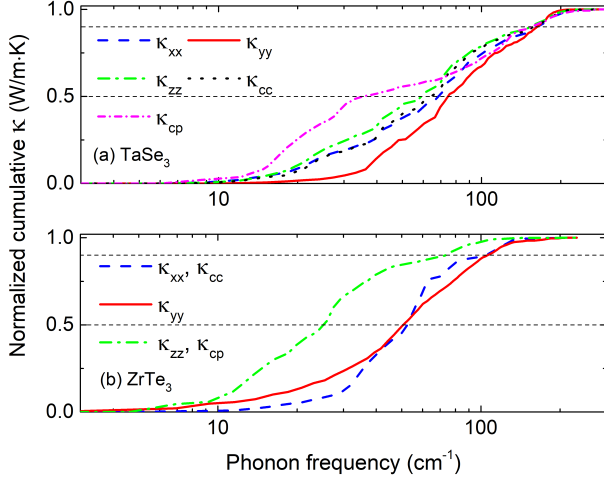


FIG. 3. Thermal conductivity values at $T = 300 \text{ K}$, normalized to their maximum values along various crystallographic directions, as cumulative functions of the phonon frequency for (a) TaSe₃ and (b) ZrTe₃. For ZrTe₃, the values for the cross-chain (cc) and cross-plane (cp) directions are indistinguishable from the values for κ_{xx} and κ_{zz} , respectively. Reference horizontal lines are at 0.5 and 0.9.

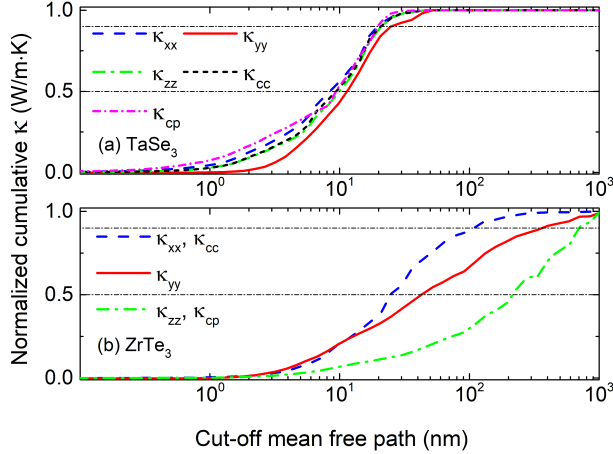


FIG. 4. Thermal conductivity values at $T = 300 \text{ K}$, normalized to its maximum value along various crystallographic directions, as functions of the cut-off mean free path for (a) TaSe₃ and (b) ZrTe₃. Reference horizontal lines are at 0.5 and 0.9.

Order-of-magnitude estimates of the electronic components of the thermal conductivities can be obtained from the Wiedemann-Franz law using the Sommerfeld value of the Lorenz number, $2.44 \times 10^{-8} \text{ W}\Omega \text{ K}^{-2}$. Values

for the Lorenz number do vary, but for room temperature metals, they tend to lie within a range of 0.6 to 2 times the Sommerfeld value. [92] Using the values for the electrical conductivities from Sec. II, the estimated room-temperature electrical component of the thermal conductivity along the chain direction for TaSe₃ is $1.2 \text{ Wm}^{-1}\text{K}^{-1}$. For ZrTe₃, the estimated room-temperature electrical component of the thermal conductivity along the chain direction ranges from 2.9 to $5.1 \text{ Wm}^{-1}\text{K}^{-1}$, and along the cross-chain direction, it ranges from 4.1 to $9.6 \text{ Wm}^{-1}\text{K}^{-1}$. For comparison, the corresponding values of the room temperature lattice thermal conductivities for TaSe₃ and ZrTe₃ along the chain direction are 6.2 and $9.6 \text{ Wm}^{-1}\text{K}^{-1}$, respectively, and for ZrTe₃ along the cross chain direction, it is $3.9 \text{ Wm}^{-1}\text{K}^{-1}$. Thus, the Wiedemann-Franz law with the Sommerfeld approximation for the Lorenz number gives room-temperature electrical components of the thermal conductivities that are on the same order as the lattice components.

To understand the contribution of the phonon modes and frequencies to the lattice thermal conductivity, we consider the room-temperature, normalized thermal conductivity as a cumulative function of phonon frequency in Fig. 3. In TaSe₃, 50% of the thermal conductivity in the chain direction (κ_{yy}) is contributed by modes with frequencies below 75 cm^{-1} . The thermal conductivity in the $a - c$ plane has a larger contribution from lower frequency phonons. In the cross-chain direction, 50% of κ_{cc} is contributed by modes with frequencies below 64 cm^{-1} , and in the cross-plane direction, 50% of κ_{cp} is contributed by modes with frequencies below 36 cm^{-1} .

In ZrTe₃, the heat is carried by lower frequency phonons than in TaSe₃. In ZrTe₃, 50% of thermal conductivity along both the chain direction (κ_{yy}) and cross-chain direction (κ_{cc}) is contributed by phonons with frequencies below 52 cm^{-1} . In the cross-plane direction 50% of κ_{cp} is contributed by modes with frequencies below 26 cm^{-1} .

For both of these materials, a significant percentage of the heat at room temperature is carried by the optical modes. This phenomenon has also recently been observed in TiS₃ [70]. Consider the chain direction, $\Gamma - Y$. In TaSe₃, essentially all of the modes above 75 cm^{-1} are optical modes, as can be seen in Fig. 1(e). Thus, approximately 50% of the heat in TaSe₃ at room temperature is carried by optical modes. In ZrTe₃, the spectrum along the chain direction above 64 cm^{-1} is composed primarily

TABLE III. Representative mean free path (λ_R) of heat carrying phonons in TaSe₃ and ZrTe₃, at $T = 300 \text{ K}$ in the 3 directions indicated in the header.

	λ_R (nm)				
	x	y	z	cross-chain	cross-plane
TaSe ₃	7.3	10.6	8.5	8.2	7.1
ZrTe ₃	25.3	43.7	178	25.3	178

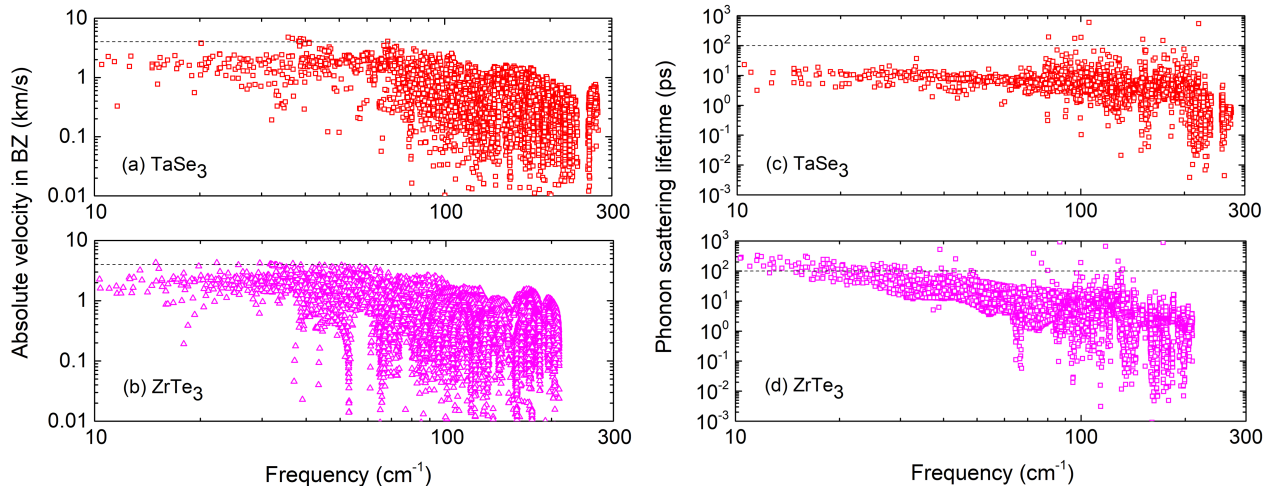


FIG. 5. Absolute velocity of phonon modes in the irreducible Brillouin zone of (a) TaSe₃ and (b) ZrTe₃. The reference horizontal lines are at 4 km/s. Scattering lifetimes of the phonon modes at $T = 300$ K for (c) TaSe₃ and (d) ZrTe₃. The reference horizontal lines are at 100 ps.

of optical modes, and it carries 33% of the heat.

Another way to analyze the physics of the heat current carried by phonons is to calculate the normalized κ as a function of the cut-off mean free path. The results are shown in Fig. 4. For TaSe₃, 90% of the thermal conductivity in the chain direction is carried by phonons with a mean free path of 25 nm or less. In both the cross-chain and cross-plane directions 90% of the thermal conductivity is carried by phonons with mean free paths of 21 nm or less. The corresponding cut-off mean free paths for ZrTe₃ are approximately an order of magnitude greater. For ZrTe₃, in the chain, cross-chain, and cross-plane directions, 90% of the heat is carried by phonons with mean free paths less than or equal to 365 nm, 110 nm, and 700 nm, respectively.

To obtain a representative mean free path (λ_R) of heat-carrying phonons, the cumulative κ with respect to the cut-off mean free path (λ_{\max}) in Fig. 4, is fitted to a single parametric function, [84, 93]

$$\kappa(\lambda_{\max}) = \frac{\kappa_0}{1 + \lambda_R/\lambda_{\max}}, \quad (4)$$

where, κ_0 is the maximum thermal conductivity. The values for λ_R for the different transport directions are tabulated in Table III. They correspond closely to the cut off mean free paths in Fig. 4 that account for 50% of the thermal conductivity in each direction. These values serve as indicators as to how and when the thermal conductivity will be affected by geometrical scaling. When dimensions are reduced below λ_R , the thermal conductivity will be reduced. The representative mean free path (λ_R) for TaSe₃ is lower than that of ZrTe₃, as shown in Table III. This is consistent with the fact that, in the low frequency ($0 \sim 50$ cm⁻¹) region, the phonon scattering

lifetimes in TaSe₃ are approximately one order of magnitude shorter than those of ZrTe₃, as discussed below and shown in Fig. 5(c,d). The cross-plane thermal conductivity of ZrTe₃ has the longest representative mean free path of 178 cm⁻¹. This is consistent with the fact that the phonons contributing to the cross-plane thermal conductivity are very low frequency (50% of the heat is carried by phonons with frequencies below 25 cm⁻¹). This frequency range is well below the optical branches, so that three phonon scattering is strongly restricted by energy and momentum conservation.

To gain further insight into why there is a significant difference between the thermal conductivity in these materials, we inspect the phonon velocity as well as the phonon lifetimes of the thermal modes. Figure 5(a,b) shows the absolute velocity distributions of the heat-carrying phonons, for each phonon mode inside the irreducible Brillouin zone (BZ), and the reference horizontal lines are at 4 km/s. The lifetimes are shown in Fig. 5(c,d), and the reference horizontal lines are at 100 ps. In the low frequency range $\lesssim 50$ cm⁻¹, ZrTe₃ has higher velocity phonons with longer lifetimes than those of TaSe₃.

In this low frequency range, the phonon lifetimes of ZrTe₃ are approximately one order of magnitude longer than those of TaSe₃. For ZrTe₃, the optical modes are close to or above 50 cm⁻¹. For TaSe₃, there are several optical branches that fall below 50 cm⁻¹ accompanied by a number of band crossings and anti-crossings. Also, since the unit cell of TaSe₃ is twice as large in the $a - c$ plane as that of ZrTe₃, there are features in the acoustic dispersion along $\Gamma - X$ and $\Gamma - Z$ that resemble zone-folding in which the acoustic branches fold back at the zone boundary and return to Γ . Both of these features result in a greater number of channels for low-frequency

phonon relaxation in TaSe₃ compared to those in ZrTe₃ and correspondingly lower phonon lifetimes. A simple illustration of how zone-folding opens new phonon relaxation channels is shown in Ref. [94].

V. SUMMARY AND CONCLUSION

The phonon dispersions and lattice thermal conductivities of TaSe₃ and ZrTe₃ are determined using density functional theory and the phonon BTE. The anisotropy of the LA acoustic phonons, as characterized by the ratios of the chain, cross-chain, and cross-plane velocities, is considerably larger in TaSe₃ than in ZrTe₃. The anisotropy of the maximum velocities of the TA modes is always less. The maximum LA velocity in ZrTe₃ occurs in the cross-chain direction, and this is consistent with the strong cross-chain bonding that gives rise to large Fermi velocities.

However, the thermal conductivity for both crystals is maximum in the chain direction. The thermal conductivity of ZrTe₃ is larger than that of TaSe₃ in each of the three directions: chain, cross-chain, and cross-plane; and it is considerably more isotropic. For TaSe₃ (ZrTe₃), the room temperature diagonal thermal conductivity values in the three directions are $\kappa_{yy} = 6.2$ (9.6), $\kappa_{cc} = 0.80$ (3.9), and $\kappa_{cp} = 0.13$ (2.3) Wm⁻¹K⁻¹.

A significant percentage of the heat at room temperature is carried by the optical phonons. In TaSe₃, the spectrum along the chain direction above 75 cm⁻¹ is composed of the optical branches and this part of the spectrum carries 50% of the heat at room temperature. In ZrTe₃, the spectrum along the chain direction above 64 cm⁻¹ is composed primarily of optical branches, and it carries 33% of the heat at room temperature. For TaSe₃ (ZrTe₃) along the chain direction at $T = 300$ K, 50% of the heat is carried by phonons below 75 (50) cm⁻¹, and this part of the phonon spectra consists primarily of the acoustic branches.

The differences between the two materials in their phonon velocities and lifetimes are most apparent in the low frequency range $\lesssim 50$ cm⁻¹. In this frequency range, the maximum phonon velocities of ZrTe₃ are approximately a factor of 2 greater than those of TaSe₃ and the phonon lifetimes in ZrTe₃ are approximately an order of magnitude greater than those in TaSe₃. The longer lifetimes result in considerably longer mean free paths in ZrTe₃ compared to those in TaSe₃. The representative mean free paths in the chain, cross-chain, and cross-plane directions for TaSe₃ (ZrTe₃) are 10.6 (43.7), 8.2 (25.3), and 7.1 (178) nm, respectively. The shorter lifetimes in the low frequency range of TaSe₃ are consistent with the presence of optical branches and zone-folding features of the acoustic branches that arise due to the doubling of the TaSe₃ unit cell in the $a - c$ plane compared to the unit cell of ZrTe₃. Both of these features serve to introduce more scattering channels for low frequency phonon relaxation.

VI. ACKNOWLEDGMENT

This work was supported in part by the NSF under Grant No EFRI-1433395. Calculations of ZrTe₃ were supported, in part, by Spins and Heat in Nanoscale Electronic Systems (SHINES) an Energy Frontier Research Center funded by the U.S. Department of Energy, Office of Science, Basic Energy Sciences under Award No DE-SC0012670. This work used the Extreme Science and Engineering Discovery Environment (XSEDE)[95], which is supported by National Science Foundation Grant No. ACI-1548562 and Allocation ID TG-DMR130081.

APPENDIX: ADDITIONAL TABLES AND FIGURES

The calculated and experimental lattice constants and angles for TaSe₃ and ZrTe₃ are provided in Table IV. The room temperature values of the diagonal elements of the thermal conductivity tensors calculated from the RTA and the full iterative approaches are listed in Table V, and the comparison for all temperatures is shown in Fig. 6. The fitting coefficients for the temperature dependent thermal conductivities $\kappa(T) = c_1 + c_2T^{-1}$ are provided in Table VI, and the plot showing the quality of the fits is given in Fig. 7. Electronic structure plots for TaSe₃ and ZrTe₃ are shown in Fig. 8. The convergence of the lattice thermal conductivities for different q -point grids is shown in Fig. 9.

TABLE IV. Lattice constants (\AA) and angles (degrees) for TaSe_3 and ZrTe_3 . The values labeled “This paper” are the values obtained after structure relaxation. The experimental values in the corresponding literature were obtained at room temperature.

Crystal	Remark	a	b	c	α	β	γ
TaSe_3	This paper	10.452	3.508	9.875	90	106.36	90
	Experiment [73, 96]	10.411	3.494	9.836	90	106.36	90
ZrTe_3	This paper	5.915	3.882	10.152	90	97.94	90
	Experiment [97]	5.895	3.926	10.104	90	97.93	90

TABLE V. Diagonal elements of the lattice thermal conductivity tensors calculated from the RTA and iterative methods at $T = 300$ K.

	Method	κ_{xx}	κ_{yy}	κ_{zz}
TaSe_3	RTA	0.3718	4.0423	0.5644
	Iterative	0.3722	6.1522	0.5643
ZrTe_3	RTA	3.6621	8.2807	2.2823
	Iterative	3.8764	9.5748	2.3435

TABLE VI. Fitting coefficients c_1 ($\text{Wm}^{-1}\text{K}^{-1}$) and c_2 (Wm^{-1}) for the temperature dependence of the diagonal elements of κ for TaSe_3 and ZrTe_3 given by the expression $\kappa = c_1 + c_2 T^{-1}$. For TaSe_3 , the coefficients for κ_{cc} and κ_{cp} are also shown. For ZrTe_3 , these are the same as κ_{xx} and κ_{zz} , respectively.

	coefficient	κ_{xx}	κ_{yy}	κ_{zz}	κ_{cc}	κ_{cp}
TaSe_3	c_1	0.003989	-0.02828	-0.003387	-0.001137	0.001768
	c_2	110.4	1880.	171.9	243.2	39.10
ZrTe_3	c_1	-0.1578	-0.1457	-0.1441	-	-
	c_2	1241	2956	772.3	-	-

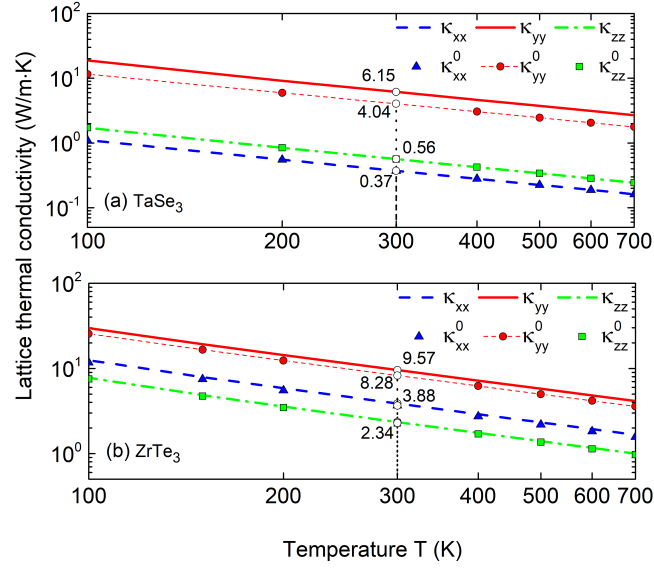


FIG. 6. Lattice thermal conductivities of (a) TaSe_3 and (b) ZrTe_3 calculated from the RTA and iterative approaches as indicated by the legends. The curves labeled κ^0 are calculated using the RTA and the curves labeled κ are calculated from the full iterative method.

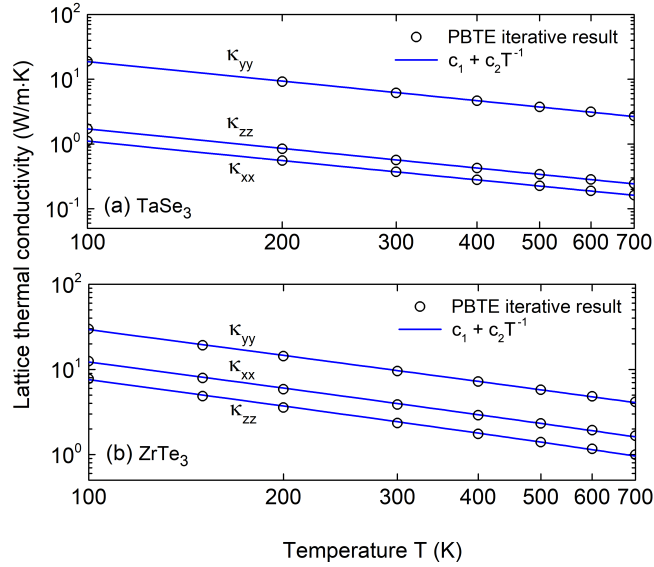


FIG. 7. Fitted thermal conductivities for (a) TaSe_3 and (b) ZrTe_3 using the coefficients listed in Table VI. The circles show the numerically calculated values, and the solid lines show the analytical fits.

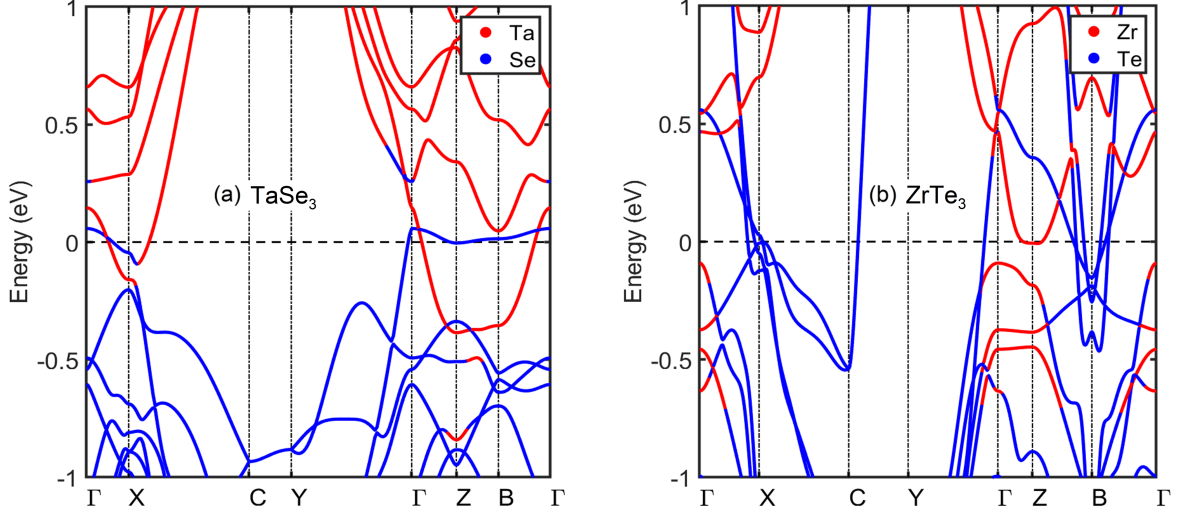


FIG. 8. Electronic structure of (a) TaSe_3 and (b) ZrTe_3 . The color indicates the dominant orbital contributions from the metal or chalcogen atoms.

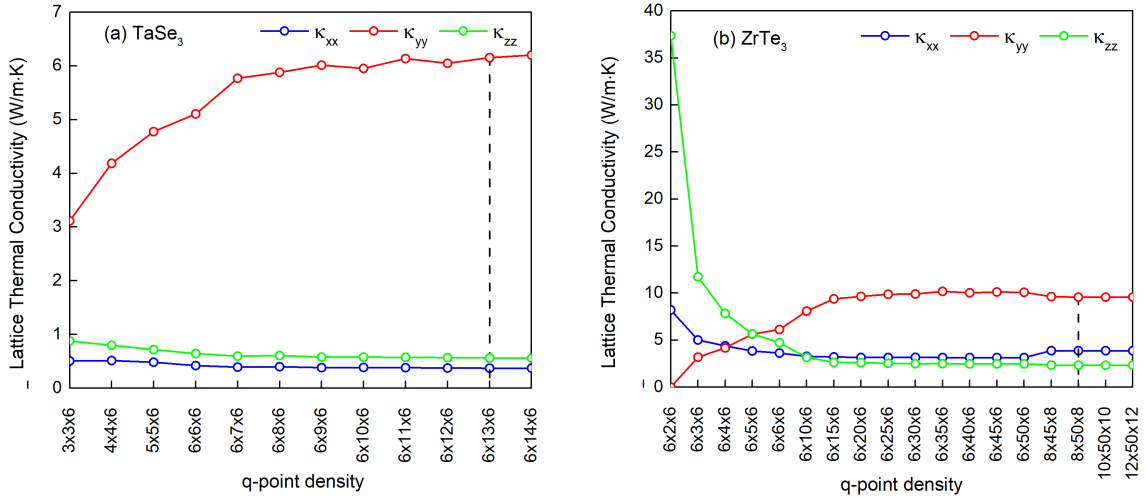


FIG. 9. Lattice thermal conductivity for (a) TaSe_3 and (b) ZrTe_3 for different q -point grids at $T = 300\text{K}$. For our calculation we have chosen a q -point of $6 \times 13 \times 6$ and $8 \times 50 \times 8$ for TaSe_3 and ZrTe_3 , respectively. The change of thermal conductivity beyond this q -point is negligible and below 1%.

-
- [1] D. W. Bullett, *J. Phys. C: Sol. St. Phys.* **12**, 277 (1979).
- [2] S. K. Srivastava and B. N. Avasthi, *J. Mat. Sci.* **27**, 3693 (1992).
- [3] J. O. Island, A. J. Molina-Mendoza, M. Barawi, R. Biele, E. Flores, J. M. Clamagirand, J. R. Ares, C. Sánchez, H. S. J. van der Zant, R. D'Agosta, I. J. Ferrer, and A. Castellanos-Gomez, *2D Mater* **4**, 022003 (2017).
- [4] S. Furuseth, L. Brattas, and A. Kjekshus, *Acta Chemica Scandinavica A* **29**, 623 (1975).
- [5] K. Endo, H. Ihara, S. Gonda, and K. Watanabe, *Physica B+ C* **105**, 159 (1981).
- [6] M.H. Rashid and D.J. Sellmyer, *Physical Review B* **29**, 2359 (1984).
- [7] Y. Jin, X. Li, and J. Yang, *Phys. Chem. Chem. Phys.* **17**, 18665 (2015).
- [8] J. Dai and X. C. Zeng, *Angew. Chem. Int. Ed.* **54**, 7572 (2015).
- [9] J. O. Island, R. Biele, M. Barawi, J. M. Clamagirand, J. R. Ares, C. Sánchez, H. S. J. van der Zant, I. J. Ferrer, R. D'Agosta, and A. Castellanos-Gomez, *Scientific Reports* **6**, 22214 (2016).
- [10] A. Pant, E. Torun, B. Chen, S. Bhat, X. Fan, K. Wu, D. P. Wright, F. M. Peeters, E. Soignard, H. Sahin, *et al.*, *Nanoscale* **8**, 16259 (2016).
- [11] J. Dai, M. Li, and X. C. Zeng, *Wiley Interdisciplinary Reviews: Computational Molecular Science* **6**, 211 (2016).
- [12] W. Kong, C. Bacaksiz, B. Chen, K. Wu, M. Blei, X. Fan, Y. Shen, H. Sahin, D. Wright, D. S. Narang, *et al.*, *Nanoscale* **9**, 4175 (2017).
- [13] T. Sambongi, M. Yamamoto, K. Tsutsumi, Y. Shiozaki, K. Yamaya, and Y. Abe, *Journal of the Physical Society of Japan* **42**, 1421 (1977).
- [14] P. Haen, F. Lapierre, P. Monceau, M. N. nez Regueiro, and J. Richard, *Solid State Communications* **26**, 725 (1978).
- [15] M. Yamamoto, *Journal of the Physical Society of Japan* **45**, 431 (1978).
- [16] K. Yamaya, S. Takayanagi, and S. Tanda, *Phys. Rev. B* **85**, 184513 (2012).
- [17] G. Grüner, *Rev. Mod. Phys.* **60**, 1129 (1988).
- [18] G. Grüner, *Density Waves in Solids* (Perseus Publishing, Boston, 1994).
- [19] P. Monceau, *Advances in Physics* **61**, 325 (2012).
- [20] V. Y. Pokrovskii, S. G. Zybtsev, M. V. Nikitin, I. G. Gorlova, V. F. Nasretdinova, and S. V. Zaitsev-Zotov, *Physics–Uspekhi* **56**, 29 (2013).
- [21] R. M. Fleming, D. E. Moncton, and D. B. McWhan, *Phys. Rev. B* **18**, 5560 (1978).
- [22] M. E. Itkis, F. Y. Nad, and P. Monceau, *J. Phys.: Condens. Matter* **2**, 8327 (1990).
- [23] S. G. Zybtsev, V. Y. Pokrovskii, V. F. Nasretdinova, S. V. Zaitsev-Zotov, V. V. Pavlovskiy, A. B. Odobesco, W. W. Pai, M.-W. Chu, Y. G. Lin, E. Zupanič, H. J. P. van Midden, S. Šturm, E. Tchernychova, A. Prodan, J. C. Bennett, I. R. Mukhamedshin, O. V. Chernysheva, A. P. Menushenkov, V. B. Loginov, B. A. Loginov, A. N. Titov, and M. Abdel-Hafiez, *Phys. Rev. B* **95**, 035110 (2017).
- [24] A. Zettl and G. Grüner, *Physical Review B* **26**, 2298 (1982).
- [25] R. P. Hall, M. F. Hundley, and A. Zettl, *Phys. Rev. B* **38**, 13002 (1988).
- [26] J. Bardeen, E. Ben-Jacob, A. Zettl, and G. Grüner, *Phys. Rev. Lett.* **49**, 493 (1982).
- [27] A. Zettl, C. M. Jackson, and G. Grüner, *Phys. Rev. B* **26**, 5773 (1982).
- [28] R. E. Thorne, W. G. Lyons, J. W. Lyding, J. R. Tucker, and J. Bardeen, *Phys. Rev. B* **35**, 6360 (1987).
- [29] H. S. J. van der Zant, E. Slot, S. V. Zaitsev-Zotov, and S. N. Artemenko, *Phys. Rev. Lett.* **87**, 126401 (2001).
- [30] S. G. Zybtsev, V. Y. Pokrovskii, V. F. Nasretdinova, and S. V. Zaitsev-Zotov, *Appl. Phys. Lett.* **94**, 152112 (2009).
- [31] S. V. Zaitsev-Zotov, *Physics Uspekhi* **47**, 533 (2004).
- [32] J. McCarten, D. A. DiCarlo, M. P. Maher, T. L. Adelman, and R. E. Thorne, *Phys. Rev. B* **46**, 4456 (1992).
- [33] H. S. J. van der Zant, A. Kalwij, O. C. Mantel, N. Markovic, Y. I. Latyshev, B. Pannetier, and P. Monceau, *J. De Physique IV* **9**, Pr10-157 (1999).
- [34] H. S. J. van der Zant, N. Marković, and E. Slot, *Physics–Uspekhi* **44**, 61 (2001).
- [35] E. Slot, H. S. J. van der Zant, K. O'Neill, and R. E. Thorne, *Phys. Rev. B* **69**, 073105 (2004).
- [36] K. Inagaki, T. Tushima, S. Tanda, and K. Yamaya, *Appl. Phys. Lett.* **86**, 073101 (2005).
- [37] Y. S. Hor, Z. L. Xiao, U. Welp, Y. Ito, J. F. Mitchell, R. E. Cook, W. K. Kwok, and G. W. Crabtree, *Nano Letters* **5**, 397 (2005).
- [38] S. G. Zybtsev and V. Y. Pokrovskii, *Phys. Rev. B* **84**, 085139 (2011).
- [39] S. Bhattacharya, A. N. Bloch, and J. P. Stokes, 'Frequency Modulator Using Material Having Sliding Charge Density Waves,' U.S. Patent 4,580,110 (1986).
- [40] T. L. Adelman, S. V. Zaitsev-Zotov, and R. E. Thorne, *Phys. Rev. Lett.* **74**, 5264 (1995).
- [41] G. Blumberg and P. B. Littlewood, 'Electronic devices based on density wave dielectrics,' U.S. Patent 6,735,073 (2004).
- [42] D. Mihailovic, D. Dvorsek, V. V. Kabanov, J. Demsar, L. Forró, and H. Berger, *Appl. Phys. Lett.* **80**, 871 (2002).
- [43] K. Stöwe and F. R. Wagner, *Journal of Solid State Chemistry* **138**, 160 (1998).
- [44] R. Seshardi, E. Suard, C. Felser, E. W. Finckh, A. Maignan, and W. Tremel, *J. Mater. Chem.* **8**, 2869 (1998).
- [45] C. Felser, E. W. Finckh, H. Kleinke, F. Rocker, and W. Tremel, *J. Mater. Chem.* **8**, 1787 (1998).
- [46] T. Yokoya, T. Kiss, A. Chainani, S. Shin, and K. Yamaya, *Phys. Rev. B* **71**, 140504(R) (2005).
- [47] M. Hoesch, A. Bosak, D. Chernyshov, H. Berger, and M. Krisch, *Phys. Rev. Lett.* **102**, 086402 (2009).
- [48] M. Hoesch, X. Cui, K. Shimada, C. Battaglia, S.-i. Fujimori, and H. Berger, *Phys. Rev. B* **80**, 075423 (2009).
- [49] Y. Hu, F. Zheng, X. Ren, J. Feng, and Y. Li, *Phys. Rev. B* **91**, 144502 (2015).
- [50] S. L. Gleason, Y. Gim, T. Byrum, A. Kogar, P. Abbamonte, E. Fradkin, G. J. MacDougall, D. J. Van Harlingen, X. Zhu, C. Petrovic, and S. L. Cooper, *Phys. Rev. B* **91**, 155124 (2015).

- [51] A. M. Ganose, L. Gannon, F. Fabrizi, H. Nowell, S. A. Barnett, H. Lei, X. Zhu, C. Petrovic, D. O. Scanlon, and M. Hoesch, *Phys. Rev. B* **97**, 155103 (2018).
- [52] M. Hoesch, L. Gannon, K. Shimada, B. J. Parrett, M. D. Watson, T. K. Kim, X. Zhu, and C. Petrovic, *Phys. Rev. Lett.* **122**, 017601 (2019).
- [53] L. Yue, S. Xue, J. Li, W. Hu, A. Barbour, F. Zheng, L. Wang, J. Feng, S. B. Wilkins, C. Mazzoli, *et al.*, *Nature communications* **11**, 1 (2020).
- [54] A. Patra and C. S. Rout, *RSC Adv.* **10**, 36413 (2020).
- [55] J. O. Island, M. Buscema, M. Barawi, J. M. Clamagirand, J. R. Ares, C. Sánchez, I. J. Ferrer, G. A. Steele, H. S. J. van der Zant, and A. Castellanos-Gomez, *Adv. Optical Mater.* **2**, 641 (2014).
- [56] J. O. Island, M. Barawi, R. Biele, A. Almazán, J. M. Clamagirand, J. R. Ares, C. Sánchez, H. S. J. van der Zant, J. V. Álvarez, R. D'Agosta, I. J. Ferrer, and A. Castellanos-Gomez, *Advanced Materials* **27**, 2595 (2015).
- [57] A. Lipatov, P. M. Wilson, M. Shekhirev, J. D. Teeter, R. Netusil, and A. Sinitskii, *Nanoscale* **7**, 12291 (2015).
- [58] S. J. Gilbert, A. Lipatov, A. J. Yost, M. J. Loes, A. Sinitskii, and P. A. Dowben, *Appl. Phys. Lett.* **114**, 101604 (2019).
- [59] M. Randle, A. Lipatov, A. Kumar, C.-P. Kwan, J. Nathawat, B. Barut, S. Yin, K. He, N. Arabchigavkani, R. Dixit, T. Komesu, J. Avila, M. C. Asensio, P. A. Dowben, A. Sinitskii, U. Singiseti, and J. P. Bird, *ACS Nano* **13**, 803 (2019).
- [60] N. Papadopoulos, E. Flores, K. Watanabe, T. Taniguchi, J. R. Ares, C. Sanchez, I. J. Ferrer, A. Castellanos-Gomez, G. A. Steele, and H. S. J. van der Zant, *2D Materials* **7**, 015009 (2019).
- [61] M. Abdulsalam and D. P. Joubert, *Eur. Phys. J. B* **88**, 177 (2015).
- [62] E. Zhang, P. Wang, Z. Li, H. Wang, C. Song, C. Huang, Z.-G. Chen, L. Yang, K. Zhang, S. Lu, *et al.*, *ACS nano* **10**, 8067 (2016).
- [63] H. Yuan, X. Liu, F. Afshinmanesh, W. Li, G. Xu, J. Sun, B. Lian, A. G. Curto, G. Ye, Y. Hikita, *et al.*, *Nature nanotechnology* **10**, 707 (2015).
- [64] M. A. Stolyarov, G. Liu, M. A. Bloodgood, E. Aytan, C. Jiang, R. Samnakay, T. T. Salguero, D. L. Nika, S. L. Rumyantsev, M. S. Shur, K. N. Bozhilov, and A. A. Balandin, *Nanoscale* **8**, 15774 (2016).
- [65] A. Geremew, M. Bloodgood, E. Aytan, B. Woo, S. Corber, G. Liu, K. Bozhilov, T. Salguero, S. Rumyantsev, M. Rao, *et al.*, *IEEE Electron Device Letters* **39**, 735 (2018).
- [66] T. A. Empante, A. Martinez, M. Wurch, Y. Zhu, A. K. Geremew, K. Yamaguchi, M. Isarraraz, S. Rumyantsev, E. J. Reed, A. A. Balandin, and L. Bartels, *Nano Letters* **19**, 4355 (2019).
- [67] M. Dresselhaus, G. Dresselhaus, X. Sun, Z. Zhang, S. Cronin, and T. Koga, *Physics of the Solid State* **41**, 679 (1999).
- [68] Z. Zhou, H. Liu, D. Fan, G. Gao, and C. Sheng, *ACS Appl. Mater. Interfaces* **10**, 37031 (2018).
- [69] M. Hooda, T. Tripathi, and C. Yadav, *Journal of Alloys and Compounds* **785**, 603 (2019).
- [70] H. Liu, X. Yu, K. Wu, Y. Gao, S. Tongay, A. Javey, L. Chen, J. Hong, and J. Wu, *Nano Letters* **20**, 5221 (2020).
- [71] T. Wieting, A. Grisel, and F. Levy, *Molecular Crystals and Liquid Crystals* **81**, 117 (1982).
- [72] A. Zwick, M. A. Renucci, and A. Kjekshus, *Journal of Physics C: Solid State Physics* **13**, 5603 (1980).
- [73] E. Bjerkelund and A. Kjekshus, *Acta Chem. Scand.* **19**, 11 (1965).
- [74] H. Nakajima, K. Nomura, and T. Sambongi, *Physica B+C* **143**, 240 (1986).
- [75] S. Takahashi, T. Sambongi, J. Brill, and W. Roark, *Solid state communications* **49**, 1031 (1984).
- [76] K. Yamaya and G. Oomi, *J. Phys. Soc. Jap.* **51**, 3512 (1982).
- [77] P. E. Blöchl, *Phys. Rev. B* **50**, 17953 (1994).
- [78] J. P. Perdew, K. Burke, and M. Ernzerhof, *Phys. Rev. Lett.* **77**, 3865 (1996).
- [79] G. Kresse and J. Hafner, *Phys. Rev. B* **48**, 13115 (1993).
- [80] G. Kresse and J. Furthmüller, *Computational Materials Science* **6**, 15 (1996).
- [81] S. Grimme, *Journal of computational chemistry* **27**, 1787 (2006).
- [82] A. Togo, F. Oba, and I. Tanaka, *Phys. Rev. B* **78**, 134106 (2008).
- [83] A. Togo and I. Tanaka, *Scr. Mater.* **108**, 1 (2015).
- [84] W. Li, J. Carrete, N. A. Katcho, and N. Mingo, *Computer Physics Communications* **185**, 1747 (2014).
- [85] W. Li and N. Mingo, *Physical Review B* **91**, 144304 (2015).
- [86] W. Li, N. Mingo, L. Lindsay, D. A. Broido, D. A. Stewart, and N. A. Katcho, *Phys. Rev. B* **85**, 195436 (2012).
- [87] T. J. Wieting, A. Grisel, F. Lévy, and P. Schmid, "Phonon studies of chemical bonding in the IVB and VB trichalcogenides," in *Lecture Notes in Physics, Quasi One-Dimensional Conductors I*, Vol. 95 (Springer-Verlag, Berlin, 1979) pp. 354–358.
- [88] B. Zawilski, R. L. IV, N. Lowhorn, and T. Tritt, *Solid State Communications* **150**, 1299 (2010).
- [89] M. Yao, M. Zebarjadi, and C. P. Opeil, *Journal of Applied Physics* **122**, 135111 (2017).
- [90] B. M. Zawilski, R. T. Littleton, and T. M. Tritt, *Review of Scientific Instruments* **72**, 1770 (2001).
- [91] L. Lindsay, D.A. Broido, and T.L. Reinecke, *Physical Review B* **88**, 144306 (2013).
- [92] G. S. Kumar, G. Prasad, and R. O. Pohl, *J. Mat. Sci.* **28**, 4261 (1993).
- [93] H. Wang, Y. Gao, and G. Liu, *RSC Adv.* **7**, 8098 (2017).
- [94] H. Li, H. Ying, X. Chen, D. L. Nika, A. I. Cocemasov, W. Cai, A. A. Balandin, and S. Chen, *Nanoscale* **6**, 13402 (2014).
- [95] J. Towns, T. Cockerill, M. Dahan, I. Foster, K. Gaither, A. Grimshaw, V. Hazlewood, S. Lathrop, D. Lifka, G. D. Peterson, *et al.*, *Computing in Science & Engineering* **16**, 62 (2014).
- [96] E. Bjerkelund and A. Kjekshus, *Zeitschrift für Anorganische und Allgemeine Chemie* **328**, 235 (1964).
- [97] H. Furuseth and S. Fjellvag, *Acta Chem. Scand.* **45**, 694 (1991).
- [98] J. Brill, C. Tzou, G. Verma, and N. Ong, *Solid State Communications* **39**, 233 (1981).
- [99] A. Smontara and K. Biljakovic, *Molecular Crystals and Liquid Crystals* **121**, 141 (1985).
- [100] J. Zhu, T. Feng, S. Mills, P. Wang, X. Wu, L. Zhang, S. T. Pantelides, X. Du, and X. Wang, *ACS Applied Materials & Interfaces* **10**, 40740 (2018).

- [101] M. K. Hooda and C. S. Yadav, *Applied Physics Letters* **111**, 053902 (2017).
- [102] G. Yumnam, T. Pandey, and A. K. Singh, *The Journal of Chemical Physics* **143**, 234704 (2015).
- [103] J.-Y. Kim, S. M. Choi, W.-S. Seo, and W.-S. Cho, *Bulletin of the Korean Chemical Society* **31**, 3225 (2010).
- [104] L. Brixner, *Journal of Inorganic and Nuclear Chemistry* **24**, 257 (1962).
- [105] Y. Nishio, *Journal of the Physical Society of Japan* **63**, 223 (1994).
- [106] M. D. Núñez-Regueiro, J. M. Lopez-Castillo, and C. Ayache, *Phys. Rev. Lett.* **55**, 1931 (1985).
- [107] Z. Yan, C. Jiang, T. R. Pope, C. F. Tsang, J. L. Stickney, P. Goli, J. Renteria, T. T. Salguero, and A. A. Balandin, *Journal of Applied Physics* **114**, 204301 (2013).
- [108] H. Imai, Y. Shimakawa, and Y. Kubo, *Physical Review B* **64**, 241104(R) (2001).